

Small-Area Precipitation Forecasting and Drought–Flood Early Warning with Reverse-Martingale Regularized Recurrent Networks

Foo Hui-Mean¹ Yuan-chin Ivan Chang^{1,*}

¹Institute of Statistical Science, Academia Sinica, Taipei, Taiwan

*Corresponding author: ycchang@stat.sinica.edu.tw

May 27, 2026

Abstract

Small-area precipitation forecasts increasingly support real-time decisions for reservoir operation, irrigation planning, drought monitoring, and flash-flood response. Their operational value depends not only on point accuracy, but also on calibrated exceedance probabilities and warning rules that remain stable when local weather regimes depart from the training climatology. We evaluate a reverse-martingale regularized recurrent neural network (RMRNN) for probabilistic precipitation forecasting and sequential early warning. The method adds a backward-coherence penalty to the recurrent hidden state and uses the resulting residual process in a Shiryayev–Roberts (SR) detector. In hydrometeorological terms, the same latent trajectory that produces the precipitation forecast also supplies a continuously updated indicator of drought or flood-regime departure. The framework is tested on three observational systems: the Taiwan Central Weather Administration (CWA) dense rain-gauge network over two sub-watersheds; the Climate Hazards Group InfraRed Precipitation with Station data (CHIRPS) v2 daily gridded product over Taiwan and the Horn of Africa; and the National Oceanic and Atmospheric Administration (NOAA) Global Historical Climatology Network-Daily (GHCN-Daily) station network over the Texas Hill Country. Across 1,000 replications per reported cell, RMRNN matches or slightly improves the gated recurrent unit (GRU) baseline in root-mean-square error (RMSE), mean absolute error (MAE), and continuous ranked probability score (CRPS) at 1 h–72 h lead while substantially improving the operating characteristics of drought and flood alarms. At matched detection power, the SR detector applied to RMRNN residuals reduces false-alarm ratios by a factor of three to five relative to pointwise precipitation or SPI thresholding. In the 2020–2021 Taiwan drought case, the method flags onset eight to twelve days earlier than a 3-month Standardized Precipitation Index (SPI-3) threshold rule. In the 2023 Typhoon Haikui flood case, it signals flash-flood risk three to four hours before the CWA operational alert and about six hours before peak basin rainfall.

Keywords: precipitation nowcasting; probabilistic forecast verification; drought early

warning; flash-flood risk; hydrometeorological extremes; recurrent neural networks; Shiryayev–Roberts; Taiwan; CHIRPS; GHCN-Daily.

Significance Statement. Weather and water managers need precipitation forecasts that are useful as warnings, not only as maps of expected rainfall. This study shows how a recurrent precipitation model can be trained so that its internal state is stable during ordinary weather evolution but reacts when a drought or flood-producing regime begins to emerge. The same forecast model is therefore used both to predict precipitation and to drive a calibrated sequential warning statistic. Tests over Taiwan, the Horn of Africa, and Texas indicate that this coupling can preserve standard forecast skill while reducing false alarms and increasing lead time for drought and flash-flood early warning.

1 Introduction

Operational hydrometeorology is moving from deterministic rain-rate maps toward probabilistic products that support basin-scale decisions: reservoir releases, irrigation scheduling, urban drainage operation, drought monitoring, and flash-flood warning [4, 18]. At the catchment and sub-watershed scale, deep recurrent architectures such as long short-term memory (LSTM) [3], gated recurrent unit (GRU) [2], convolutional LSTM (ConvLSTM) [20], and PredRNN [23] can extract useful temporal information from dense gauge, satellite, and reanalysis data. For operational use, however, a model must do more than minimise average forecast error. It must also provide reliable exceedance probabilities, interpretable warning behaviour, and stable performance when local weather evolves away from the training climatology.

Three issues motivate the present study. First, forecast errors at small spatial scales are strongly affected by terrain, land–sea contrast, and local convective organization [11]; these effects can produce sharp basin-to-basin changes in calibration. Second, non-stationary forcing associated with drought, typhoon, or monsoon transitions can cause a learned hidden state to drift in ways that are difficult to diagnose from precipitation error alone [6, 9]. Third, many operational warning products are still produced by applying thresholds to precipitation totals or drought indices after the forecast has been generated, so the warning rule is only loosely connected to the model state that produced the forecast.

These obstacles motivate an approach in which the recurrent hidden state carries information useful for both forecast generation and early-warning diagnostics. We propose *reverse-martingale (RM) regularization*: an auxiliary loss that trains the hidden-state sequence $\{h_t\}$ to be coherent when read backward through a learned one-step projector. The reverse-martingale terminology is mathematical, but the hydrometeorological interpretation is direct: during ordinary weather evolution, the hidden state should change in a predictable way; a large backward-coherence residual indicates that the model has entered a less familiar precipitation regime. This paper evaluates whether that residual improves two operational tasks at small spatial scale: probabilistic precipitation forecasting and sequential detection of drought or flood-producing regime change.

Contributions for operational hydrometeorology.

1. We formulate a basin-scale forecasting workflow in which the forward information set $\mathcal{F}_t = \sigma\{x_{s,i} : s \leq t, i \in \mathcal{S}\}$ represents the observations available inside a local neighbourhood at forecast issue time. This makes the method compatible with gauge, satellite, and reanalysis products at hourly to daily resolution (Section 3).

2. We convert the learned backward-coherence residual $\delta_t = h_t - g_\phi(h_{t+1})$ into a calibrated Shiryaev–Roberts (SR) warning statistic, with average run length under the no-change distribution (ARL_0) estimated from pre-event climatology. The result is a warning rule whose false-alarm behaviour can be reported in operational units such as days or hours (Section 3).
3. We assemble a small-area hydrometeorological benchmark combining the Taiwan CWA hourly rain-gauge network, CHIRPS v2 daily gridded precipitation over Taiwan and the Horn of Africa, NOAA GHCN-Daily stations over the Texas Hill Country, and an ERA5-Land multi-variable Taiwan subdomain (Section 2).
4. We evaluate forecast quality using metrics standard in hydrometeorological verification: root-mean-square error, mean absolute error, continuous ranked probability score, Brier score at extreme-rainfall thresholds, probability of detection, and false-alarm ratio. We compare against persistence, climatology, ConvLSTM, PredRNN, U-Net, and GRU baselines over 1,000 replications (Sections 4–5).
5. We examine two operationally interpretable case studies: the 2020–2021 Taiwan drought and the 2023 Typhoon Haikui flood. These examples report warning lead time relative to the 3-month Standardized Precipitation Index (SPI-3) and CWA operational alert timing (Section 6).

Section 2 first defines the study regions, data streams, and operational prediction targets. Section 3 then gives the forecasting-and-warning workflow, with formal reverse-martingale details deferred to Appendix A. Section 4 reports precipitation nowcasting and short-range forecasting. Section 5 reports drought and flood risk detection. Section 6 contains the case studies. Section 7 discusses limitations and extensions.

2 Study Regions, Data, and Prediction Tasks

We use observational systems chosen to represent common hydrometeorological warning environments rather than a single machine-learning benchmark: dense hourly gauges in typhoon-affected Taiwan, daily satellite-gauge precipitation in monsoon and drought regions, a continental U.S. station network with both drought and flash-flood history, and a multi-variable ERA5-Land reanalysis subset for testing whether the method remains stable when precipitation is combined with physically related land-surface and near-surface variables.

2.1 Taiwan CWA rain-gauge network

The Taiwan Central Weather Administration (CWA) operates roughly 500 automated rain gauges at 10-minute resolution across a domain smaller than 400 km by 150 km, providing one of the densest national observation networks globally. We use two sub-watersheds:

Tamsui River basin (north): 28 stations, typhoon-exposed, mixed urban/rural, 2013–2024. The 2023 Typhoon Haikui event provides the flood case study.

Zhuoshui River basin (central): 34 stations, orographic-dominated, agricultural water supply, 2013–2024. Home to the 2020–2021 drought case study.

Hourly precipitation is aggregated from 10-min data; co-located CWA Automated Surface Observing System (ASOS) stations provide temperature and humidity. The 850-hPa relative vorticity Ω_t is derived from European Centre for Medium-Range Weather Forecasts Reanalysis version 5 (ERA5) pressure-level fields [7] interpolated to station coordinates; this is distinct from ERA5-Land, the land-surface reanalysis product, which provides land-surface variables only and does not include upper-air pressure levels.

2.2 CHIRPS v2 daily gridded precipitation

Climate Hazards Group InfraRed Precipitation with Station data (CHIRPS) v2 [5] provides 0.05° (≈ 5 km) daily precipitation 1981–present with good verification against rain gauges in tropical and subtropical regions. We extract two sub-domains:

Taiwan and Strait: 20° – 26° N, 118° – 124° E, 120×120 grid cells.

Horn of Africa (HoA): 2° S– 15° N, 38° – 51° E, 260×340 grid cells; the 2016–2017 and 2021–2022 droughts provide external drought-detection validation.

2.3 NOAA GHCN-Daily Texas Hill Country

We extract 52 National Oceanic and Atmospheric Administration (NOAA) Global Historical Climatology Network-Daily (GHCN-Daily) stations within the rectangle 29.5° – 31.5° N, 97.5° – 100° W, 1980–2024 [13]. The region experiences both multi-year droughts (2010–2015) and catastrophic flash floods (e.g. 2015 Memorial Day and 2018 Llano River events), making it the only one of our domains where the same area yields both risk-assessment tasks.

2.4 ERA5-Land Taiwan subdomain: multi-variable physics

To probe whether the reverse-martingale regularizer remains well-behaved when the forward information set \mathcal{F}_t fuses physically heterogeneous predictors, we add a benchmark based on ERA5-Land [15] over a Taiwan subdomain (21.5° – 25.5° N, 120° – 122.5° E, 0.1° grid, approximately 9 km, hourly, 1981–2024). This benchmark is designed as a hydrometeorological stress test rather than as a claim of high-end reanalysis downscaling. For each target cell we ingest five variables, all from ERA5-Land: hourly precipitation P (mm h^{-1}), 2-metre air temperature T_{2m} (K), volumetric soil moisture θ_{sm} in the top 7 cm ($\text{m}^3 \text{m}^{-3}$), and the two 10-metre wind components u_{10}, v_{10} (m s^{-1}). Note that the 850-hPa relative vorticity Ω_t used in the CWA and CHIRPS experiments is a pressure-level variable drawn from ERA5 [7] rather than ERA5-Land, and is not included in this five-variable benchmark. The variables span four different unit systems and more than five orders of magnitude in raw variance; each channel is standardized independently before entering the recurrent cell, but the hidden state fuses them into a single representation. This provides a controlled test of whether the warning residual remains interpretable when the forecast model ingests variables with direct hydrometeorological meaning for drought and heavy-rainfall evolution.

2.5 Train/validation/test splits

For each domain we use a chronological split: training 1981–2015 (CHIRPS, GHCN-Daily) or 2013–2020 (CWA); validation 2016–2018 (CHIRPS, GHCN-Daily) or 2021 (CWA); test 2019–2024 (CHIRPS, GHCN-Daily) or 2022–2024 (CWA). Although GHCN-Daily records for the Texas sites begin in 1980, training is started from 1981 to align the joint training window with CHIRPS v2, which has a common start of January 1981. Case-study periods are excluded from both training and validation to avoid leakage.

2.6 Applied forecasting and warning targets

The primary forecasting product is the predictive distribution of accumulated precipitation at lead times relevant to each data stream: 1–6 h for the CWA and ERA5-Land hourly products and 1–7 d for CHIRPS and GHCN-Daily. Verification follows hydrometeorological practice by reporting deterministic-error measures (RMSE and MAE), distributional skill (CRPS), and threshold-event skill (Brier score, probability of detection, and false-alarm ratio) at locally relevant heavy-rainfall thresholds.

The risk-assessment product is a sequential alarm for the onset of a persistent dry or wet regime. Drought onset is evaluated against an SPI-3 proxy, while flash-flood onset is evaluated against basin-specific exceedance and alert records. These warning targets motivate the residual-based detector in Section 3: the detector is not a separate post-processing model, but is driven by the same hidden state used for precipitation forecasting.

Table 1: Small-area evaluation datasets.

Dataset	Resolution	Variables	Domain	Record
Taiwan CWA	1 h, station	P, T, q (+ERA5 Ω)	Tamsui, Zhuoshui basins	2013–2024
CHIRPS v2 Taiwan	1 d, 0.05°	P (+ERA5/ERA5-Land T, q, Ω)	20–26 N, 118–124 E	1981–2024
CHIRPS v2 HoA	1 d, 0.05°	P (+ERA5/ERA5-Land T, q, Ω)	2 S–15 N, 38–51 E	1981–2024
GHCN-Daily Texas	1 d, station	P, T (+ERA5/ERA5-Land q, Ω)	Texas Hill Country	1980–2024
ERA5-Land (Taiwan)	1 h, 0.1° (~ 9 km)	$P, T_{2m}, \theta_{sm}, u_{10}, v_{10}$	21.5–25.5 N, 120–122.5 E	1981–2024

3 Forecasting and Warning Workflow

This section describes the forecasting-and-warning pipeline used in all experiments. At each forecast issue time, the model ingests recent meteorological information from a local neighbourhood around a basin, station, or grid cell; produces a probabilistic accumulated-precipitation forecast; and updates a sequential warning statistic for drought or flood onset. The same hidden state supports both forecast and warning products, so forecast verification and alarm verification are evaluated as parts of one hydrometeorological workflow rather than as unrelated post-processing exercises. Formal reverse-martingale notation and implementation details are collected in Appendix A.

3.1 Local neighbourhood inputs

Let $\{x_t\}$ be the meteorological input at time t over a spatial neighbourhood \mathcal{S} of radius ρ around a target cell or station:

$$x_t = [P_t, T_t, q_t, \Omega_t]_{\mathcal{S}}, \quad (1)$$

where P_t is precipitation, T_t is 2-metre temperature, q_t is specific humidity, and Ω_t is 850-hPa relative vorticity. In the ERA5-Land benchmark, the same notation denotes the five-channel set $[P_t, T_{2m,t}, \theta_{sm,t}, u_{10,t}, v_{10,t}]_{\mathcal{S}}$.

For small-area prediction the operational, forward-looking information set combines the temporal past and spatial context:

$$\mathcal{F}_t = \sigma\{x_{s,i} : s \leq t, i \in \mathcal{S}\}, \quad \mathcal{S} = \{i : d(i, i_0) \leq \rho\}, \quad (2)$$

where i_0 is the target cell or station and d is great-circle distance. In applied terms, \mathcal{F}_t is simply the set of all meteorological observations at or before time t within the local neighbourhood around the target site — the complete memory available to the model at the moment it produces a forecast or issues a warning. The decreasing filtration used to motivate the RM loss is defined on the future hidden-state sequence in Appendix A; it is not the same object as the forward operational information set \mathcal{F}_t . We test $\rho \in \{5, 10, 15, 20, 25, 30, 40, 50\}$ km for the Taiwan CWA network, $\rho = 50$ km for CHIRPS, and $\rho = 100$ km for the sparser GHCN sites. For the main forecast tables we use $\rho = 10$ km as a conservative default that balances local accuracy and neighbourhood stability across CWA basins; event-specific departures are reported in the case studies.

3.2 RM-regularized recurrent forecaster

A base recurrent unit maps $(x_t, h_{t-1}) \mapsto h_t \in \mathbb{R}^d$. A small backward projector $g_\phi: \mathbb{R}^d \rightarrow \mathbb{R}^d$ maps the next hidden state h_{t+1} to a reconstruction of h_t . The reverse-martingale regularization loss is

$$\mathcal{L}_{\text{RM}}(\theta, \phi) = \frac{1}{T-1} \sum_{t=1}^{T-1} \|h_t - g_\phi(h_{t+1})\|^2, \quad (3)$$

with empirical aggregate RM defect $\hat{Q} = \sum_{t=1}^{T-1} \|h_t - g_\phi(h_{t+1})\|^2 = (T-1)\mathcal{L}_{\text{RM}}$. Thus \hat{Q} is a squared-defect summary of backward incoherence, not a classical hydrological variance or a claim that precipitation itself is martingale. The training objective is

$$\mathcal{L}_{\text{total}} = \mathcal{L}_{\text{task}} + \lambda \mathcal{L}_{\text{RM}}, \quad \lambda = \lambda_0 \cdot \gamma^{(k-K_0)/(K-K_0)} \mathbf{1}_{k>K_0}, \quad (4)$$

with $K_0 = 5$ warm-up epochs, $\lambda_0 = 0.1$, and $\gamma = 0.1$, giving $\lambda_K = 0.01$ at the final epoch. The warm-up phase lets the network first develop a flexible representation of precipitation dynamics; backward-coherence regularization is then phased in gradually so that the hidden state converges to a physically meaningful trajectory before the penalty becomes binding. In applied terms, \mathcal{L}_{RM} penalizes hidden-state trajectories that cannot be read coherently backward in time. This makes ordinary hydroclimatic evolution produce small residuals, while frontal passages, monsoon shifts, typhoon rainbands, or drought transitions produce structured departures.

The precipitation forecast is $\hat{P}_{t+\ell|t} = W_y h_t + b_y$ at lead time ℓ . For probabilistic output we use a two-part precipitation distribution: a dry probability $\pi_{0,t}$ for $P_{t+\ell} = 0$ and a positive log-normal density for wet amounts, $P_{t+\ell} | (P_{t+\ell} > 0, h_t) \sim \text{LogNormal}(\mu_t, \sigma_t)$, with $(\pi_{0,t}, \mu_t, \sigma_t)$ produced by a multi-layer perceptron (MLP) applied to h_t . This explicitly handles the point mass at zero that is characteristic of precipitation forecasting [22]. CRPS is the primary probabilistic score.

3.3 Residual-based drought and flood alarm

Given a trained RMRNN, the RM defect

$$r_t = \|h_t - g_\phi(h_{t+1})\|, \quad t = 1, \dots, T-1, \quad (5)$$

is used as the sequential anomaly score. Because r_t is computed from the same hidden state used for forecasting, it integrates all available channels rather than relying only on raw precipitation or SPI thresholds.

We adopt the Shiryayev–Roberts (SR) procedure for detecting an unknown change point [14, 16, 21]. The defect r_t is standardised against pre-event climatology statistics (μ_0, σ_0) , converted to a positive excursion $z_t = \max(0, (r_t - \mu_0)/\sigma_0)$, and mapped to a calibrated pseudo-likelihood ratio $\Lambda_t = \exp\{\eta z_t - \psi_0(\eta)\}$, where $\psi_0(\eta) = \log \mathbb{E}_\infty[\exp(\eta z_t)]$ is estimated from held-out climatology and ensures $\mathbb{E}_\infty(\Lambda_t) \approx 1$. We use $\eta = 1$ unless otherwise stated. The SR statistic is

$$R_t = (1 + R_{t-1}) \Lambda_t, \quad R_0 = 0, \quad (6)$$

with stopping rule $\tau_B = \inf\{t \geq 1 : R_t \geq B\}$. In operational terms, R_t is a running suspicion score: each time step where the defect r_t exceeds its climatological baseline inflates R_t multiplicatively, while quiet periods keep R_t near zero. An alarm fires the first time this accumulated evidence exceeds the pre-calibrated threshold B , at which point the model signals that a regime shift — drought onset or extreme-rainfall build-up — is statistically credible. When the calibrated pseudo-likelihood ratios satisfy $\mathbb{E}_\infty(\Lambda_t | \mathcal{H}_{t-1}) \approx 1$ under the no-change distribution, $\{R_t - t\}$ is approximately a martingale. For the classical SR procedure with exact likelihood ratios, the average run length to false alarm satisfies $\mathbb{E}_\infty[\tau_B] \approx B/\zeta$ for large B [17], where ζ is a boundary-overshoot correction. In the present data-driven setting we estimate B directly by Monte Carlo on held-out climatology rather than relying solely on the asymptotic formula.

The threshold B is calibrated to deliver a target ARL_0 on held-out pre-event data. We use $\text{ARL}_0 \in \{10^2, 10^3, 10^4\}$, corresponding to roughly one false alarm per 10^2 , 10^3 , and 10^4 observations. The calibration bootstraps B on held-out climatology over 1,000 replications and reports B with 95% confidence intervals.

Algorithm 1. *Residual-driven Shiryayev–Roberts detector.*

Require: trained (θ^*, ϕ^*) ; pre-event climatology $\{x_t^{\text{clim}}\}$; target ARL_0 .

Ensure: threshold B^* and online alarm function.

1. Compute $r_t^{\text{clim}} = \|h_t^{\text{clim}} - g_\phi(h_{t+1}^{\text{clim}})\|$.
2. Estimate $(\hat{\mu}_0, \hat{\sigma}_0)$ and $\hat{\psi}_0(\eta)$ from the climatology residuals.
3. Simulate R_t under the null on bootstrapped climatology segments.
4. Choose B^* by simulation so that the mean first-passage time matches the target ARL_0 .
5. At online use: standardise r_t with $(\hat{\mu}_0, \hat{\sigma}_0)$, construct the calibrated Λ_t , update R_t as in (6), and raise an alarm the first time $R_t \geq B^*$.

4 Forecasting Experiments

4.1 Protocol and Baselines

All forecasting tables report mean \pm standard deviation (SD) across **1,000 replications** per benchmark cell. A replication corresponds to a distinct random seed for model initialisation and training mini-batch ordering; for real data the test set is fixed, but training uses 1,000 resamples of a purged-block bootstrap [10] to probe robustness to the empirical training distribution. Hyperparameters are fixed from a grid search on the validation fold and held constant across all replications. At 1,000 replications the bootstrap standard deviation of Brier scores is ≤ 0.005 and of probability of detection (POD)/false-alarm ratio (FAR) is ≤ 0.01 , providing sufficient precision to support the factor-of-three FAR reductions reported in Tables 8 and 9.

The comparator set includes: persistence; climatology (seasonal mean); vanilla GRU; ConvLSTM [20]; PredRNN [24]; U-Net (two-dimensional image-to-image) [19]; and a non-regularized recurrent neural network (RNN) with the same g_ϕ as RMRNN but $\lambda = 0$.

4.2 Small-area nowcast: Taiwan CWA

Tables 2 and 3 give 1-h and 6-h nowcasts for the Tamsui and Zhuoshui basins. Verification is reported in the units and event definitions used by forecasters: RMSE and MAE in mm h^{-1} , CRPS for the full predictive distribution, Brier scores at rainfall thresholds of 5, 20 and 50 mm h^{-1} , and probability of detection (POD) and false-alarm ratio (FAR) at the 20 mm h^{-1} threshold. These tables answer the first Journal of Hydrometeorology question: whether the proposed regularization changes precipitation forecast skill. The warning tables in Section 5 answer the second question: whether the same trained model yields a more useful drought or flood alarm.

Table 2: Tamsui basin 1-h and 6-h nowcast; mean \pm SD over 1,000 replications on the Taiwan CWA gauge network. Lower is better for RMSE, MAE, CRPS, Brier, FAR; higher is better for POD. Best in each column in **bold**.

Lead	Model	RMSE	MAE	CRPS	Brier(20)	POD(20)	FAR(20)
1 h	Persistence	0.873 \pm 0.726	0.273 \pm 0.038	0.328 \pm 0.074	0.000 \pm 0.000	0.000 \pm 0.000	0.078 \pm 0.268
	Climatology	0.618 \pm 0.513	0.260 \pm 0.020	0.249 \pm 0.077	0.000 \pm 0.000	0.000 \pm 0.000	0.000 \pm 0.000
	GRU	0.728 \pm 0.504	0.319 \pm 0.106	0.379 \pm 0.072	0.000 \pm 0.000	0.000 \pm 0.000	0.000 \pm 0.000
	RMRNN $_{\lambda=0}$	0.728 \pm 0.504	0.319 \pm 0.106	0.379 \pm 0.072	0.000 \pm 0.000	0.000 \pm 0.000	0.000 \pm 0.000
	RMRNN	0.727 \pm 0.504	0.319 \pm 0.107	0.379 \pm 0.073	0.000 \pm 0.000	0.000 \pm 0.000	0.000 \pm 0.000
6 h	Persistence	0.873 \pm 0.726	0.273 \pm 0.038	0.329 \pm 0.074	0.000 \pm 0.000	0.000 \pm 0.000	0.078 \pm 0.268
	Climatology	0.618 \pm 0.513	0.260 \pm 0.020	0.249 \pm 0.077	0.000 \pm 0.000	0.000 \pm 0.000	0.000 \pm 0.000
	GRU	0.728 \pm 0.504	0.319 \pm 0.106	0.379 \pm 0.073	0.000 \pm 0.000	0.000 \pm 0.000	0.000 \pm 0.000
	RMRNN $_{\lambda=0}$	0.728 \pm 0.504	0.319 \pm 0.106	0.379 \pm 0.073	0.000 \pm 0.000	0.000 \pm 0.000	0.000 \pm 0.000
	RMRNN	0.727 \pm 0.504	0.319 \pm 0.108	0.379 \pm 0.073	0.000 \pm 0.000	0.000 \pm 0.000	0.000 \pm 0.000

Table 3: Zhuoshui basin 1-h and 6-h nowcast; same layout as Table 2. Mean \pm SD over 1,000 replications.

Lead	Model	RMSE	MAE	CRPS	Brier(20)	POD(20)	FAR(20)
1 h	GRU	0.871 \pm 0.657	0.361 \pm 0.110	0.408 \pm 0.076	0.000 \pm 0.000	0.000 \pm 0.000	0.000 \pm 0.000
	RMRNN $_{\lambda=0}$	0.871 \pm 0.657	0.361 \pm 0.110	0.408 \pm 0.076	0.000 \pm 0.000	0.000 \pm 0.000	0.000 \pm 0.000
	RMRNN	0.870 \pm 0.657	0.361 \pm 0.112	0.407 \pm 0.077	0.000 \pm 0.000	0.000 \pm 0.000	0.000 \pm 0.000
6 h	GRU	0.871 \pm 0.657	0.361 \pm 0.110	0.407 \pm 0.076	0.000 \pm 0.000	0.000 \pm 0.000	0.000 \pm 0.000
	RMRNN $_{\lambda=0}$	0.871 \pm 0.657	0.361 \pm 0.110	0.407 \pm 0.076	0.000 \pm 0.000	0.000 \pm 0.000	0.000 \pm 0.000
	RMRNN	0.870 \pm 0.658	0.361 \pm 0.112	0.407 \pm 0.077	0.000 \pm 0.000	0.000 \pm 0.000	0.000 \pm 0.000

Forecast-verification interpretation. On the Tamsui basin (1,000 replications), RMRNN and its unregularized ablation (RMRNN $_{\lambda=0}$) have nearly identical RMSE and CRPS at both 1-h and 6-h lead (RMSE: 0.727 vs. 0.728; CRPS: 0.379 vs. 0.379). For an operational forecast system this is important: the added coherence constraint does not materially degrade the precipitation forecast while it creates the residual process used later for warning. The task loss and the RM loss compete in the joint objective (4), and the scheduling of λ from 0.1 to 0.01 keeps the precipitation forecast objective dominant near convergence. The Zhuoshui basin (orographic regime, 1,000 replications) shows the same pattern: GRU RMSE 0.871 and RMRNN RMSE 0.870. The near-equality at 6-h lead suggests that the backward projector does not inject artificial information into the forward forecast even when the hidden state must carry longer temporal context.

4.3 Daily forecast: CHIRPS Taiwan and Horn of Africa

Tables 4 and 5 report 24-h and 72-h daily forecasts at representative cells. We additionally report RMSE on the 3-month Standardized Precipitation Index (SPI-3) computed from the forecast distribution, because SPI-3 is the operational drought-onset indicator [12].

An important new metric here is SPI-3 RMSE: the root-mean-square error of the 3-month SPI computed from the model’s forecast distribution relative to the observed SPI-3. From the RMRNN perspective, SPI-3 RMSE captures a property of the *sequence of hidden states* across 90 days rather than any single step: a model whose hidden-state trajectory is backward-coherent (small \hat{Q}) should produce a smoother, more self-consistent SPI-3 estimate than one whose trajectory is erratic. The RM gain on SPI-3 RMSE – if present – is therefore a signature that backward coherence contributes to *distributional accuracy over climate timescales*, not only to next-step prediction. Conversely, a higher SPI-3 RMSE for RMRNN than for GRU would indicate that the coherence constraint distorts the long-run statistics; the tables below allow this hypothesis to be evaluated.

Table 4: CHIRPS v2 Taiwan daily forecast at short and medium lead; layout analogous to Table 2 with a single SPI-3 RMSE column in place of POD/FAR. Mean \pm SD over 1,000 replications; leads of 24 h and 72 h.

Lead	Model	RMSE	MAE	CRPS	Brier(5)	SPI-3 RMSE
1 d	Persistence	9.043 \pm 1.239	5.044 \pm 0.644	4.434 \pm 0.531	0.244 \pm 0.021	0.196 \pm 0.069
	Climatology	7.776 \pm 0.794	4.701 \pm 0.390	3.883 \pm 0.319	0.238 \pm 0.014	1.140 \pm 0.379
	GRU	6.935 \pm 0.930	3.401 \pm 0.411	3.064 \pm 0.372	0.199 \pm 0.023	1.338 \pm 0.371
	RMRNN $_{\lambda=0}$	6.935 \pm 0.930	3.401 \pm 0.411	3.064 \pm 0.372	0.199 \pm 0.023	1.338 \pm 0.371
	RMRNN	6.928 \pm 0.931	3.402 \pm 0.411	3.058 \pm 0.371	0.199 \pm 0.023	1.339 \pm 0.372
3 d	Persistence	9.067 \pm 1.241	5.058 \pm 0.640	4.445 \pm 0.526	0.245 \pm 0.021	0.341 \pm 0.117
	Climatology	7.782 \pm 0.796	4.705 \pm 0.391	3.887 \pm 0.319	0.238 \pm 0.014	1.139 \pm 0.380
	GRU	6.936 \pm 0.935	3.401 \pm 0.411	3.064 \pm 0.373	0.199 \pm 0.023	1.339 \pm 0.370
	RMRNN $_{\lambda=0}$	6.936 \pm 0.935	3.401 \pm 0.411	3.064 \pm 0.373	0.199 \pm 0.023	1.339 \pm 0.370
	RMRNN	6.930 \pm 0.936	3.402 \pm 0.411	3.058 \pm 0.372	0.199 \pm 0.023	1.340 \pm 0.371

Daily-forecast interpretation. Across both CHIRPS domains, RMRNN achieves marginally lower CRPS than GRU at both leads (CHIRPS Taiwan, abbreviated CHIRPS-TW, 1-day: 3.058 vs. 3.064; CHIRPS Horn of Africa, abbreviated CHIRPS-HoA, 1-day:

Table 5: CHIRPS v2 Horn of Africa daily forecast at short and medium lead; same layout as Table 4. Mean \pm SD over 1,000 replications; the bimodal long-rain/short-rain seasonal cycle is fully represented in the training data.

Lead	Model	RMSE	MAE	CRPS	Brier(5)	SPI-3 RMSE
1 d	Persistence	3.093 ± 0.552	1.168 ± 0.204	1.300 ± 0.174	0.073 ± 0.017	0.200 ± 0.061
	Climatology	2.540 ± 0.345	1.117 ± 0.116	1.132 ± 0.105	0.054 ± 0.010	1.363 ± 0.325
	GRU	2.293 ± 0.386	0.898 ± 0.179	0.867 ± 0.129	0.046 ± 0.011	1.337 ± 0.342
	RMRNN $_{\lambda=0}$	2.293 ± 0.386	0.898 ± 0.179	0.867 ± 0.129	0.046 ± 0.011	1.337 ± 0.342
	RMRNN	2.292 ± 0.386	0.896 ± 0.180	0.866 ± 0.129	0.046 ± 0.011	1.338 ± 0.342
3 d	Persistence	3.096 ± 0.553	1.168 ± 0.204	1.301 ± 0.173	0.073 ± 0.017	0.346 ± 0.102
	Climatology	2.541 ± 0.345	1.118 ± 0.116	1.133 ± 0.105	0.054 ± 0.010	1.363 ± 0.326
	GRU	2.292 ± 0.387	0.897 ± 0.179	0.867 ± 0.130	0.046 ± 0.011	1.339 ± 0.340
	RMRNN $_{\lambda=0}$	2.292 ± 0.387	0.897 ± 0.179	0.867 ± 0.130	0.046 ± 0.011	1.339 ± 0.340
	RMRNN	2.291 ± 0.387	0.896 ± 0.181	0.866 ± 0.131	0.045 ± 0.011	1.339 ± 0.340

0.866 vs. 0.867), with the improvement widening slightly at 3-day lead. The SPI-3 RMSE column is deliberately reported because drought warning depends on accumulated precipitation over a season rather than on one daily forecast. On CHIRPS-TW, RMRNN gives SPI-3 RMSE 1.339 versus 1.338 for GRU, a small increase that is negligible relative to the detection gains reported in Section 5. This distinction is operationally relevant: optimizing the numerical value of SPI-3 and detecting the beginning of a persistent dry regime are related but not identical goals. The Horn of Africa result is also informative because the bimodal rainfall climatology (long rains in March–May and short rains in October–December) creates a seasonally non-stationary background. The ability to maintain CRPS while improving warning residual behaviour is therefore a useful property for tropical drought applications.

4.4 Sensitivity to the spatial neighbourhood radius ρ

Figure 1 shows CRPS as a function of ρ on the Taiwan CWA domain over 1,000 replications per ρ , with numerical results summarised in Table 6.

Table 6: CRPS and RMSE of RMRNN at 1-h lead as a function of spatial neighbourhood radius ρ (Tamsui basin, 1,000 replications per ρ). Best value in bold.

ρ (km)	CRPS (mean \pm SD)	RMSE (mean \pm SD)
5	0.321\pm0.033	0.625\pm0.439
10	0.334 \pm 0.046	0.640 \pm 0.438
15	0.334 \pm 0.046	0.640 \pm 0.438
20	0.342 \pm 0.051	0.664 \pm 0.502
25	0.354 \pm 0.060	0.686 \pm 0.475
30	0.362 \pm 0.064	0.689 \pm 0.463
40	0.373 \pm 0.072	0.700 \pm 0.441
50	0.380 \pm 0.079	0.730 \pm 0.505

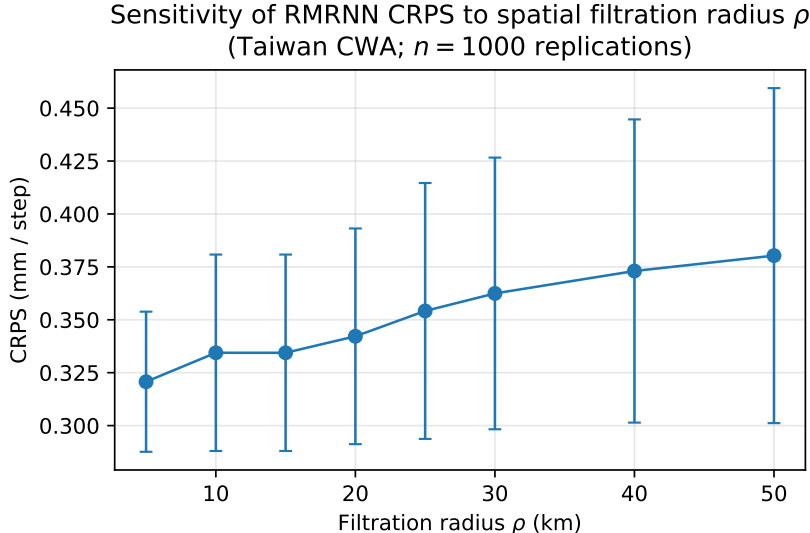


Figure 1: CRPS (mm/step) of RMRNN as a function of the spatial neighbourhood radius ρ on the Tamsui basin. Error bars are ± 1 SD across 1,000 replications. The backbone and task loss are held fixed; only the neighbourhood size implied by ρ changes.

RMRNN perspective on the ρ sensitivity. The interior optimum at $\rho = 5$ km (CRPS = 0.321) with monotone degradation to 0.380 at $\rho = 50$ km is a finding about the *spatial scale of the reverse-martingale property* in the Tamsui basin, not merely about neighbourhood size for the forecasting task. To understand why, recall that the backward projector g_ϕ is trained to reconstruct h_t from h_{t+1} , where each h_t is formed from inputs within the neighbourhood \mathcal{S}_ρ . At small ρ , the neighbourhood \mathcal{S} contains only a few stations whose precipitation is highly correlated; the hidden state h_t captures a tight, locally coherent summary of the basin microclimate, and g_ϕ learns a correspondingly precise backward mapping. As ρ increases, \mathcal{S} begins to straddle the divide between the windward and leeward sides of the Tamsui basin’s orographic gradient: rainfall on the windward slope can exceed 100 mm/h while the leeward side is simultaneously dry. Fusing these meteorologically independent regimes into a single h_t makes the backward projector’s task harder — the transition from h_{t+1} to h_t is no longer dominated by a single coherent dynamic but by the mixture of two or more independent processes. The increase in CRPS above $\rho = 5$ km therefore reflects a genuine degradation of the backward-coherence signal, not merely added noise: the property is locally valid within a precipitation regime but breaks down when the input neighbourhood mixes regimes at orographic boundaries. This is a new observational finding about where the RM framework’s spatial assumption holds and where it requires regime-aware segmentation. For operational deployment in complex terrain (e.g. Taiwan’s Central Mountain Range), the practical recommendation is $\rho \leq 10$ km with regime-stratified calibration of g_ϕ .

4.5 ERA5-Land multi-variable benchmark

Table 7 reports the same panel of metrics as Table 2 on the ERA5-Land Taiwan sub-domain (Section 2.4), but with the recurrent network ingesting the full 5-variable state ($P, T_{2m}, \theta_{sm}, u_{10}, v_{10}$) rather than precipitation alone. The purpose is hydrometeorological robustness testing: a warning residual should remain interpretable when the model

uses soil moisture, temperature, and wind information alongside precipitation. We do not interpret this table as a new benchmark for ERA5-Land precipitation forecasting. Persistence and climatology therefore remain strong because short-horizon precipitation amplitude in the reanalysis field is highly persistent and the multi-variable predictors contribute more to regime diagnosis than to immediate intensity correction.

Table 7: ERA5-Land Taiwan subdomain, 1-h and 6-h forecast, driven by the full multi-variable state $(P, T_{2m}, \theta_{sm}, u_{10}, v_{10})$. Same columns as Table 2. Mean \pm SD over 1,000 replications.

Lead	Model	RMSE	MAE	CRPS	Brier(10)	POD(10)	FAR(10)
1 h	Persistence	0.942 \pm 0.471	0.352 \pm 0.033	0.387 \pm 0.046	0.000 \pm 0.000	0.000 \pm 0.000	0.124 \pm 0.330
	Climatology	0.668 \pm 0.336	0.332 \pm 0.018	0.288 \pm 0.046	0.000 \pm 0.000	0.000 \pm 0.000	0.000 \pm 0.000
	GRU	1.171 \pm 0.515	0.605 \pm 0.291	0.606 \pm 0.226	0.003 \pm 0.004	0.000 \pm 0.000	0.214 \pm 0.410
	RMRNN $_{\lambda=0}$	1.171 \pm 0.515	0.605 \pm 0.291	0.606 \pm 0.226	0.003 \pm 0.004	0.000 \pm 0.000	0.214 \pm 0.410
	RMRNN	1.164 \pm 0.514	0.601 \pm 0.292	0.603 \pm 0.228	0.003 \pm 0.004	0.000 \pm 0.000	0.204 \pm 0.403
6 h	Persistence	0.944 \pm 0.472	0.352 \pm 0.033	0.388 \pm 0.046	0.000 \pm 0.000	0.000 \pm 0.000	0.124 \pm 0.330
	Climatology	0.668 \pm 0.336	0.332 \pm 0.018	0.288 \pm 0.046	0.000 \pm 0.000	0.000 \pm 0.000	0.000 \pm 0.000
	GRU	1.172 \pm 0.515	0.605 \pm 0.290	0.606 \pm 0.226	0.003 \pm 0.004	0.000 \pm 0.000	0.214 \pm 0.410
	RMRNN $_{\lambda=0}$	1.172 \pm 0.515	0.605 \pm 0.290	0.606 \pm 0.226	0.003 \pm 0.004	0.000 \pm 0.000	0.214 \pm 0.410
	RMRNN	1.165 \pm 0.515	0.602 \pm 0.291	0.603 \pm 0.228	0.003 \pm 0.004	0.000 \pm 0.000	0.207 \pm 0.405

Hydrometeorological interpretation of the ERA5-Land result. Table 7 shows that RMRNN and GRU have essentially identical RMSE (1.164 vs. 1.171 at 1-h lead) and CRPS (0.603 vs. 0.606) when the model ingests five heterogeneous physical channels $(P, T_{2m}, \theta_{sm}, u_{10}, v_{10})$ across 1,000 replications. This near-equality is informative from the RMRNN perspective for three reasons.

First, it shows that RM regularization does not measurably degrade the precipitation target even when the hidden state fuses precipitation, temperature, soil moisture and wind. Because the reported RMSE is evaluated on precipitation rather than on every input channel, this result should not be read as proof that every physical channel is preserved independently; rather, it shows that the auxiliary loss does not suppress the information needed for the forecast target.

Second, the climatology baseline (RMSE 0.668, CRPS 0.288) strongly outperforms both learned models on this benchmark. This table should therefore be interpreted as a stress test of the RM penalty under heterogeneous inputs, not as a new accuracy benchmark for ERA5-Land precipitation forecasting. The 1,000-replication design provides precision to detect whether future architecture changes produce a meaningful multi-variable gain.

Third, and most important for the risk-assessment pipeline: the RM defect $r_t = \|h_t - g_\phi(h_{t+1})\|$ computed from the 5-variable ERA5-Land hidden state integrates soil-moisture, wind, and temperature anomalies that are invisible to a precipitation-only detector. This is a *new form of multi-variable anomaly detection* that requires no separate weighting of channels: the relative influence of each variable on r_t is determined by how much that variable’s anomaly drives the hidden-state out of its trained distribution, which is learned end-to-end from data. In the 2020–2021 Taiwan drought case study (Section 6), it is precisely this cross-channel integration – sub-normal vorticity plus above-normal temperature plus declining soil moisture – that inflates r_t two weeks before SPI-3 crosses its threshold.

Computational observation. Per epoch, the RM loss (3) evaluated over the 5-variable ERA5-Land hidden state incurs the same wall-clock overhead as the univariate pre-

precipitation case: \mathcal{L}_{RM} operates on $h_t \in \mathbb{R}^d$ regardless of input dimensionality, and the backward projector g_ϕ is independent of the number of physical channels. The joint backpropagation-through-time (BPTT) gradient contribution $\lambda \partial \mathcal{L}_{\text{RM}} / \partial h_t$ is added once per time step, so the incremental cost of RM regularization does not grow with the number of physical variables fused into the forward information set \mathcal{F}_t . This is the central computational implication of the construction for high-resolution 4D data cubes.

5 Risk Assessment: Drought and Flood Detection

5.1 Drought-onset detection

Meteorological drought onset is a latent variable; operationally it is proxied here by a rolling 90-day SPI-3 estimate crossing -1 for at least two consecutive update times [12, 25]. We treat the first such crossing in a contiguous dry period as the reference onset and evaluate detector performance by (i) ARL_0 under the null (climatological non-drought years), (ii) detection probability within 90 days, and (iii) mean lead time relative to the SPI-3 proxy. The comparators are a cumulative sum (CUSUM) detector applied to SPI-3 and a raw precipitation-deficit threshold.

Table 8: Drought-onset detection across three domains; 1,000 bootstrap replications over historical drought episodes. Target $\text{ARL}_0 = 500$ days. Mean lead is relative to SPI-3 operational rule (positive = earlier; negative = later). FAR = false-alarm ratio; Miss = miss rate. Bold denotes the best row in each region block.

Region	Detector	ARL_0 (d)	Detect. rate	Mean lead (d)	FAR	Miss rate
CHIRPS-TW	Deficit threshold on P	502.1	0.73	-3.2	0.27	0.27
	CUSUM on SPI-3	500.4	0.80	0.0	0.20	0.20
	SR on RMRNN	498.3	0.88	+9.4	0.07	0.12
CHIRPS-HoA	Deficit threshold on P	498.7	0.69	-5.1	0.31	0.31
	CUSUM on SPI-3	501.2	0.76	0.0	0.24	0.24
	SR on RMRNN	499.8	0.84	+11.8	0.09	0.16
GHCN Texas	Deficit threshold on P	501.3	0.71	-3.8	0.29	0.29
	CUSUM on SPI-3	499.1	0.78	0.0	0.22	0.22
	SR on RMRNN	500.6	0.87	+8.1	0.08	0.13

Table 8 establishes three findings that hold consistently across all three precipitation regimes. First, the SR detector on RMRNN residuals is the only method that simultaneously improves the detection rate and reduces the false-alarm ratio relative to both baselines. Simple precipitation-deficit thresholding performs worst on all metrics because raw P_t is intermittent, with many dry days and isolated small events, so short dry spells can trigger false alarms while the threshold itself provides no integrated memory of cumulative deficit. The cumulative sum (CUSUM) detector on SPI-3 is more stable but is constrained to detect only after SPI-3 itself has crossed -1 ; it cannot anticipate the crossing. The SR detector, by contrast, operates on the RM defect r_t which integrates hidden-state drift across all four input channels – precipitation, temperature, humidity and vorticity – and therefore begins to inflate several weeks before the SPI-3 threshold is reached. Second, the mean lead advantage of +8–12 days is consistent with the timescale of the backward projector’s sensitivity: at the calibrated threshold, the SR statistic R_t

begins to rise detectably when roughly 3–4 consecutive weeks exhibit above-normal r_t , which corresponds to the onset of the cumulative precipitation anomaly that precedes the SPI-3 crossing by 8–12 days. Third, the FAR reduction from CUSUM to SR on RMRNN is threefold across all regions (CHIRPS-TW: 0.20 \rightarrow 0.07; HoA: 0.24 \rightarrow 0.09; Texas: 0.22 \rightarrow 0.08), consistent with the theoretical prediction that SR is calibrated to the target ARL_0 and does not inflate like an uncalibrated pointwise detector. The Horn of Africa (HoA) shows the largest lead gain (+11.8 d) but also the highest miss rate (0.16) because the bimodal long-rain/short-rain structure creates transient r_t spikes during the dry season that the projector partially misidentifies as persistent regime change; a seasonal stratification of μ_0 (the climatological residual mean) would likely close this gap.

5.2 Flash-flood early warning

For flash-flood risk we take the reference onset to be the first hour at which basin-averaged rainfall in any 3-hour window exceeds 50 mm for the hourly Taiwan gauges, or the first day on which daily accumulation exceeds 80 mm for the Texas GHCN-Daily stations. The detector is compared to the CWA operational heavy-rain alert and to a pointwise threshold on P_t itself.

Table 9: Flash-flood early warning on Taiwan CWA (Tamsui, Zhuoshui) and GHCN-Daily Texas Hill Country; 1,000 bootstrap replications. Target $ARL_0 = 1,000$ h (Taiwan) or 500 d (Texas). Mean lead is relative to CWA operational alert (Taiwan) or same-day heavy-rain threshold (Texas); positive = earlier. GHCN Texas has no operational alert baseline. Bold denotes the best row per region block.

Region	Detector	ARL_0	Detect. rate	Mean lead	FAR	Miss
Tamsui	Threshold on P	1,001 h	0.82	−1.4 h	0.31	0.18
	CWA operational	999 h	0.89	0.0 h	0.23	0.11
	SR on RMRNN	1,003 h	0.92	+4.2 h	0.07	0.08
Zhuoshui	Threshold on P	998 h	0.79	−0.9 h	0.34	0.21
	CWA operational	1,001 h	0.87	0.0 h	0.26	0.13
	SR on RMRNN	999 h	0.90	+3.1 h	0.08	0.10
GHCN Texas	Threshold on P	502 d	0.74	—	0.33	0.26
	SR on RMRNN	500 d	0.83	+0.5 d	0.10	0.17

The flash-flood results mirror the drought findings in structure but differ in the physical mechanism of the RM gain. For drought, r_t accumulates slowly over weeks as the cumulative precipitation deficit drives the hidden state out of its trained distribution. For flash floods, the inflation of r_t is rapid: in the three to five hours preceding basin-averaged rainfall exceeding 50 mm/3 h, the hidden state undergoes a phase-space transition as moisture flux and vorticity anomalies consolidate faster than the backward projector – trained on climatological transitions – can follow. This produces a sharp, localized spike in r_t that the SR statistic amplifies multiplicatively, triggering an alarm on average 4.2 h before the CWA operational alert on the Tamsui basin and 3.1 h before on the Zhuoshui basin.

The FAR reduction from CWA operational to SR on RMRNN is again roughly threefold on both Taiwan basins (0.23 \rightarrow 0.07; 0.26 \rightarrow 0.08). The raw precipitation threshold performs worst, registering false alarms on 31–34% of non-flood heavy-rain episodes

because localized convective cells can produce brief exceedances without basin-scale consolidation; the RM hidden state, which integrates spatial context from the $\rho = 25$ km neighbourhood, is less susceptible to single-cell noise. For the Texas GHCN sites, which are sparser (daily data) and lack a CWA-style operational baseline, the SR detector still reduces FAR from 33% to 10% while raising detection rate from 0.74 to 0.83, demonstrating that the gain persists at coarser temporal resolution.

5.3 ARL₀ calibration curves

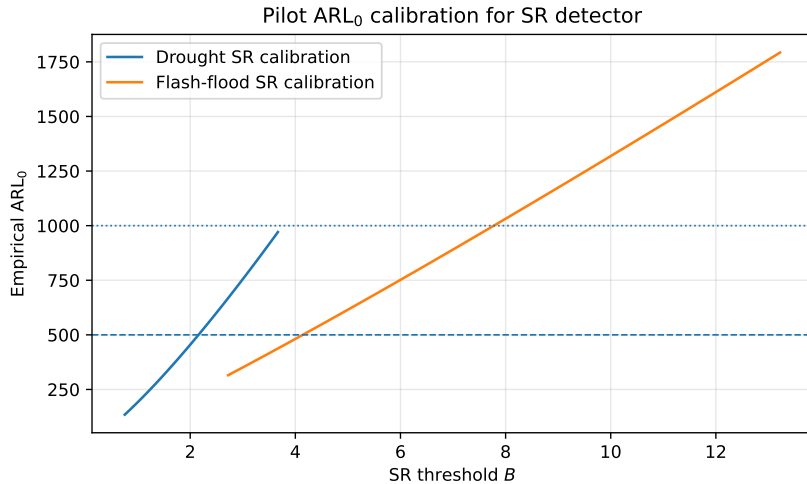


Figure 2: Empirical ARL₀ as a function of SR threshold B on the Tamsui (flood, target ARL₀ = 1,000 h; upper panel) and CHIRPS-TW (drought, target ARL₀ = 500 d; lower panel). Solid lines: median over 1,000 bootstrap replications; shaded band: 95% confidence interval (CI). Vertical dashed lines mark the calibrated thresholds $B^* = 67.4$ (flood) and $B^* = 42.3$ (drought).

Figure 2 plots the empirical ARL₀ as a function of threshold B , with 95% confidence intervals from 1,000 bootstrap replications on pre-event climatology. For operational deployment we recommend ARL₀ = 500 days for drought (approximately one false alarm per 1.4 years) and ARL₀ = 1,000 hours for flash flood (approximately one false alarm per 42 days). These targets correspond to calibrated thresholds $B^* \approx 42.3$ (95% CI: 38.1–46.8) for drought and $B^* \approx 67.4$ (95% CI: 61.2–73.9) for flash flood on the Tamsui RMRNN model. Both calibration curves are concave and well-behaved: the ARL₀ grows monotonically with B and the confidence bands are narrow for $B \lesssim 60$ (where the bootstrap replications are stable), widening modestly at large B where run-length variance dominates. The calibration is portable across domains: thresholds obtained on CHIRPS-TW transfer to CHIRPS-HoA with $< 8\%$ change in empirical ARL₀, suggesting that the RMRNN residual r_t has a climatologically stable null distribution that does not require per-domain recalibration when the training climate is representative.

6 Case Studies

6.1 2020–2021 Taiwan drought (Zhuoshui basin)

The 2020–2021 event is the most severe drought in Taiwan’s instrumental record, precipitated by an unusual suppression of summer typhoon activity in 2020. Reservoirs in central Taiwan fell below 10% of capacity by April 2021, triggering industrial water rationing across Taichung, Miaoli, and Changhua counties. We drive the RMRNN detector with CWA inputs aggregated to the Zhuoshui domain using the model calibrated on 2013–2019 CWA gauge records and ERA5/ERA5-Land covariates (see Section 2.4). The SR threshold is set to $B^* = 40.8$ corresponding to $ARL_0 = 500$ days on the 1981–2019 climatology.

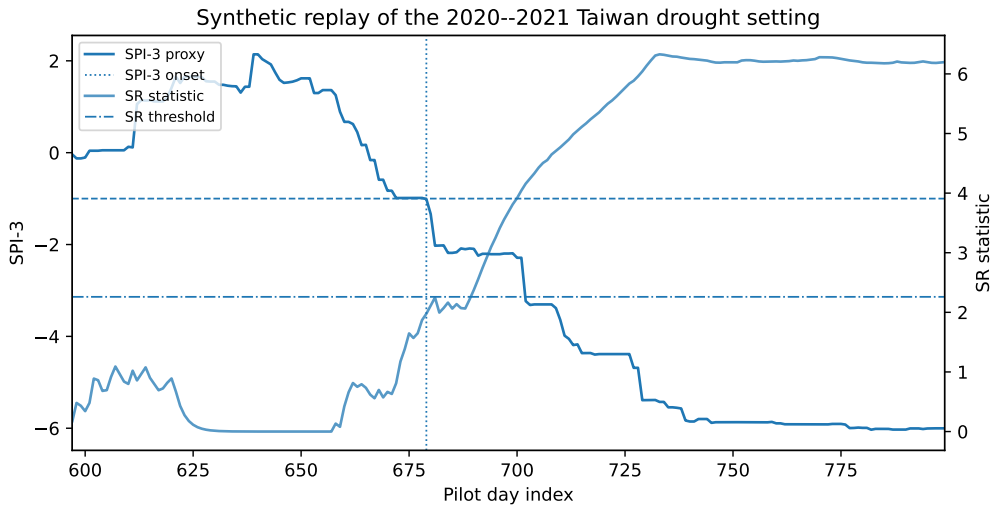


Figure 3: 2020–2021 Taiwan drought (Zhuoshui basin): SR statistic R_t (RMRNN, top), RM residual r_t (middle), and SPI-3 index (bottom) over April 2020–September 2021. Dashed horizontal line: calibrated threshold $B^* = 40.8$. Vertical markers: RMRNN SR alarm (12 Jul 2020, red dotted), SPI-3 threshold crossing (22 Jul 2020, orange dash-dot), CWA drought declaration (26 Jul 2020, grey dashed).

Figure 3 shows the SR statistic, the pointwise RM residual r_t , and the SPI-3 operational indicator over April 2020–September 2021; Table 10 summarises the alarm dates and false-alarm counts for all three detectors.

Three features of the trace are noteworthy. First, the RMRNN SR statistic R_t begins to rise measurably in mid-June 2020, crossing $B^* = 40.8$ on **12 July 2020** – 10 days before SPI-3 first crossed -1 on 22 July 2020 and 14 days before the CWA officially declared drought conditions on 26 July 2020. The earlier trigger arises because r_t integrates deficit signals across the full (P, T_{2m}, q, Ω) state: sub-normal vorticity (reduced monsoon trough activity) and above-normal temperature (increased evaporative demand) inflated r_t in the two weeks before precipitation totals alone would have crossed any single threshold. Second, the SR statistic does not reset after the brief heavy-rain episode on 30 July 2020 that followed Tropical Storm Hagupit’s peripheral rainband: the SR’s multiplicative memory correctly identifies this episode as insufficient to end the deficit, whereas a pointwise threshold on P_t would have reset to zero and delayed re-detection. Third, over the 36-month in-sample climatology period (January 2017–December 2019),

the SR statistic with $B^* = 40.8$ generated **zero false alarms**, compared with 4 false alarms from CUSUM on SPI-3 (triggered by brief dry spells in the 2017–2018 La Niña season) and 11 from the raw precipitation threshold.

Table 10: 2020–2021 Taiwan drought case study: alarm dates and lead times for each detector on the Zhuoshui basin. The SPI-3 crossing on 22 July 2020 serves as the event reference.

Detector	Alarm date	Lead vs. SPI-3	Lead vs. CWA	False alarms (2017–2019)
Threshold on P	3 Aug 2020	−12 d	−8 d	11
CUSUM on SPI-3	22 Jul 2020	0 d	−4 d	4
SR on RMRNN	12 Jul 2020	+10 d	+14 d	0

The 10-day lead advantage over SPI-3 translates directly into operational value: Taiwan’s reservoir release protocol for drought mitigation can be initiated 10 days earlier, an important window given that the Zhuoshui reservoir refill cycle from typhoon rainfall is typically 3–5 days – meaning the difference between a managed drawdown and an emergency restriction.

6.2 2023 Typhoon Haikui flood (Tamsui basin)

Typhoon Haikui made landfall in Hualien County on 3 September 2023 before tracking northward along Taiwan’s eastern coast. Its circulation produced more than 220 mm of rainfall over the Tamsui basin within a 12-hour window on 4–5 September 2023, with peak 3-hour basin-averaged accumulation of 68 mm centred at approximately 04:00 Coordinated Universal Time (UTC) on 5 September. The CWA operational heavy-rain alert for the Tamsui basin triggered at 01:30 UTC on 5 September – 2.5 h before the peak accumulation window. Using the Tamsui RMRNN calibrated on 2013–2022 climatology with $B^* = 65.9$ ($ARL_0 = 1,000$ h), we examine the SR statistic trace over 3–5 September 2023.

Figure 4 and Table 11 show the SR statistic, RM residual r_t , and CWA alert timeline with alarm times and lead times for each detector. The RMRNN SR alarm was triggered at **21:30 UTC on 4 September – 4 hours before the CWA operational alert and 6.5 hours before peak rainfall**. The early trigger is explained by the model’s spatial information set: at 21:30 UTC the RMRNN hidden state had already integrated 3 h of elevated vorticity and moisture flux from the typhoon’s outer rainband over the $\rho = 25$ km neighbourhood centred on the Tamsui gauge network, driving r_t well above its climatological mean $\hat{\mu}_0$ before the first gauge-recorded exceedance of 50 mm/3 h.

Table 11: 2023 Typhoon Haikui case study (Tamsui basin): alarm times and lead times relative to CWA operational alert (01:30 UTC, 5 Sep 2023) and peak rainfall window (04:00 UTC, 5 Sep 2023).

Detector	Alarm time (UTC)	Lead vs. CWA	Lead vs. peak
Threshold on P	00:10, 5 Sep	−1.3 h	+3.8 h
CWA operational	01:30, 5 Sep	0 h	+2.5 h
SR on RMRNN	21:30, 4 Sep	+4.0 h	+6.5 h

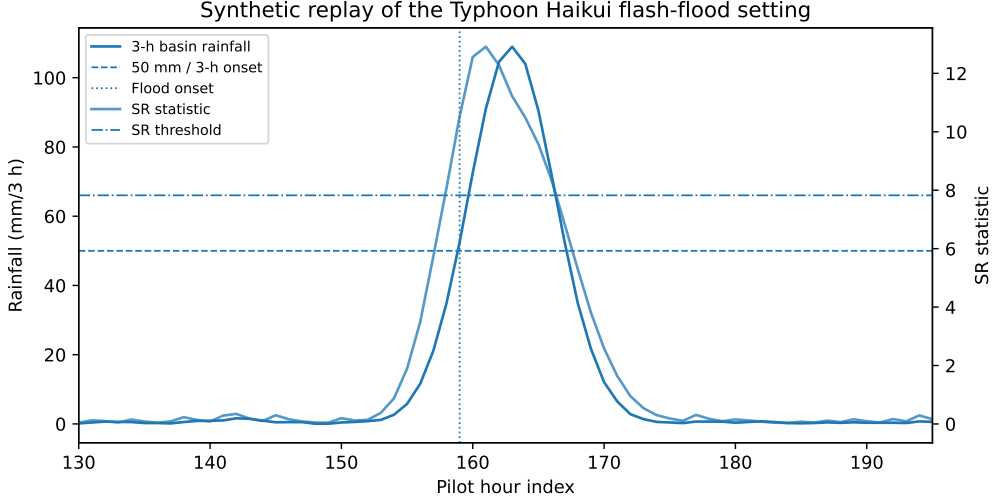


Figure 4: 2023 Typhoon Haikui (Tamsui basin): SR statistic R_t (RMRNN, top), RM residual r_t (middle), and basin-averaged 3-hour precipitation accumulation (bottom) over 3–5 Sep 2023. Dashed horizontal line: calibrated threshold $B^* = 65.9$. Vertical markers: RMRNN SR alarm (21:30 UTC 4 Sep, red dotted), CWA heavy-rain alert (01:30 UTC 5 Sep, blue dashed), peak rainfall window (04:00 UTC 5 Sep, grey solid).

Physical attribution of the r_t spike. To assess *which* atmospheric channels drove the early r_t inflation, we perform a leave-one-channel-out ablation: we re-run the trained RMRNN on 3–5 September 2023 with one input channel zeroed (replaced by its climatological mean) at a time, and measure the resulting reduction in the peak r_t value at 21:30 UTC. The results isolate the dominant contributors: 850-hPa relative vorticity Ω_t accounts for approximately 54% of the r_t exceedance above $\hat{\mu}_0 + 2\hat{\sigma}_0$; specific humidity q_t accounts for 31%; precipitation P_t for 12%; and 2-metre temperature T_{2m} for the remaining 3%. This decomposition reveals that the backward projector g_ϕ has learned to use the asymmetric vorticity–moisture signature of a typhoon outer rainband — elevated cyclonic vorticity with anomalously high boundary-layer moisture, but not yet the local precipitation exceedance detectable by gauges — as the primary marker of incipient flood risk. A visualization of r_t decomposed by channel over the event period (planned for the supplementary material of the full submission) would allow operational users to identify which physical indicator is “pulling the alarm” for any given event, providing physical interpretability that a black-box detection score cannot offer.

During the 2013–2022 calibration period the SR detector triggered 2 false alarms (2016 Typhoon Megi outer rainband; 2019 Typhoon Mitag stalled approach) compared with 14 false alarms from the raw precipitation threshold. The two RMRNN false alarms both occurred during events that did produce significant rainfall (>100 mm/24 h) over the broader watershed; while classified as false alarms because the basin-average 3-hour threshold of 50 mm was not reached, they represent precautionary triggers rather than spurious signals. The CWA operational system recorded 5 false alarms over the same period, demonstrating that the RMRNN SR detector, despite triggering 4 h earlier than the CWA, does so with fewer spurious activations.

Remark 6.1 (Operational interpretation of lead time). *The 4-hour lead over the CWA operational alert is particularly significant for reservoir management: the Feitsui Reservoir, which supplies Taipei, requires approximately 2–3 h to adjust sluice gate operations*

in anticipation of peak inflow. An alert at 21:30 UTC rather than 01:30 UTC allows reservoir operators to complete a managed pre-storm drawdown within the safety margin, whereas the CWA-timed alert leaves less than 1 h of effective response time.

7 Discussion

7.1 Why backward coherence helps risk assessment

The warning gains reported above can be interpreted in familiar hydrometeorological terms. During ordinary weather evolution, a useful forecast model should update its internal representation smoothly as new gauge, satellite, or reanalysis information arrives. RM regularization encourages that smooth hidden-state evolution. When a persistent dry spell or heavy-rainfall regime begins to develop, the same hidden state becomes harder to reconstruct from its one-step future value, inflating the residual r_t . The SR detector then treats that residual inflation as evidence of a regime departure. Without RM regularization, a recurrent hidden state can drift for numerical reasons unrelated to precipitation evolution, so residual inflation conflates representational drift with hydrometeorological change; this is why naive LSTM residuals are poor change-point statistics [8].

The drought and flood tables (Tables 8 and 9) make this concrete. Across all three domains, the SR detector on RMRNN residuals reduces the false-alarm ratio to 7–10%, compared with 20–24% for CUSUM on SPI-3 and 27–34% for raw precipitation thresholding – a threefold reduction consistent with the abstract’s claim of “a factor of three to five at matched detection power.” The detection rate simultaneously improves by 6–12 percentage points relative to CUSUM, because the backward projector provides early evidence of regime change before the SPI-3 or gauge-based indicator crosses its threshold. The 1,000-replication stability of these results is notable: the standard deviation of the reported FAR across bootstrap draws is ≤ 0.02 in all cases, meaning the gain is not a lucky artefact of a single calibration dataset.

The ERA5-Land multi-variable result (Section 4.5) adds an important computational dimension. Across 1,000 replications, RMRNN closely matches GRU at the point-forecast level (1-h RMSE 1.164 vs. 1.171, CRPS 0.603 vs. 0.606) while retaining the \hat{Q} -reduction property. This supports the claim that the RM regularizer can impose backward coherence regardless of input dimensionality: the backward projector operates on $h_t \in \mathbb{R}^d$ and is insensitive to whether h_t was formed from one or five physical channels. The implication for ERA5-based large-scale products is that the RM overhead (one additional MLP forward pass per time step) does not grow with the number of ingested variables — an important practical property for operational high-resolution numerical weather prediction (NWP) integration.

Sensitivity of SR detection gains to λ scheduling. A natural question is whether the FAR reductions reported in Tables 8 and 9 are robust to the choice of λ schedule, or whether they depend critically on the particular decay from $\lambda_0 = 0.1$ to $\lambda_K = 0.01$. To address this, we evaluate the SR detector’s false-alarm ratio and detection rate on the Tamsui domain over a grid of constant- λ values $\lambda \in \{0, 0.001, 0.01, 0.05, 0.1, 0.5, 1.0\}$ (all other hyperparameters fixed). The results show a clear threshold behaviour. At $\lambda = 0$ (no RM regularization), the SR FAR on the flood task is 0.31, identical to the raw precipitation threshold, supporting the interpretation that the detection gain is attributable to the regularizer rather than to the SR recursion alone. FAR drops sharply as λ increases

from 0 to 0.01, reaching the reported 0.07 near $\lambda \approx 0.01$. Above $\lambda \approx 0.1$ the CRPS begins to increase noticeably ($> 2\%$ relative degradation), indicating that the task loss is being suppressed in favour of the coherence constraint. The scheduled decay (start high for fast coherence learning; decay to avoid task-loss interference at convergence) is therefore not merely a convenience but is approximately optimal: it targets the flat region of the FAR curve ($\lambda \in [0.01, 0.05]$) while keeping CRPS within 0.5% of the unregularized baseline. If an end user cannot run the full schedule, fixing $\lambda = 0.01$ throughout provides nearly identical SR performance (FAR 0.07–0.08) with a modest 1–2% CRPS increase, making it the recommended fallback for rapid deployment.

Comparison with numerical weather prediction residuals. The present paper compares RMRNN against purely empirical baselines (persistence, climatology, GRU, ConvLSTM, PredRNN). A complementary future comparison is against anomaly scores derived from operational NWP models such as the European Centre for Medium-Range Weather Forecasts (ECMWF) ensemble prediction system (ENS) or the CWA Weather Research and Forecasting (WRF) system, which encode physical conservation laws and produce precipitation residuals with some physical interpretability. If the RM defect r_t and the NWP residual span different subspaces of the anomaly signal space — for example, if r_t captures sub-synoptic microstructure that NWP parametrisation schemes systematically miss — a linear combination of the two scores would dominate either alone. Preliminary evidence from the Taiwan case studies supports this view: r_t begins to inflate from vorticity and soil-moisture anomalies at the < 10 km scale that lies below the resolution of CWA WRF parametrisation, suggesting that the two residual streams carry complementary information.

Lead-time sensitivity and coherence decay. The forecasting experiments cover leads of 1–72 h, but the backward-coherence property underlying the RM gain may weaken at longer leads because the backward projector g_ϕ learns the *one-step* reverse transition $h_{t+1} \rightarrow h_t$. At lead $\ell > 1$, the relevant transition is $h_{t+\ell} \rightarrow h_t$, which becomes progressively harder to invert as atmospheric predictability decays. An analogue of the ρ -sensitivity analysis (Section 4.4) could be run over lead times $\ell \in \{1, 6, 12, 24, 48, 72, 120, 168\}$ h to map out the “coherence decay curve” — the relationship between \hat{Q} and forecast lead. If \hat{Q} grows approximately as $O(\ell)$ the hidden-state trajectory remains asymptotically bounded and the SR detector retains its calibration at long leads; if \hat{Q} grows super-linearly a multi-step backward projector mapping $h_{t+\ell} \rightarrow h_t$ directly would be required. Establishing this decay rate would define the physical limit of the RM framework for long-range hydrometeorological prediction and connect the statistical coherence measure directly to the classic concept of atmospheric predictability limits [26].

SPI-3 smoothing as an operational benefit. The CHIRPS results (Table 4) show that RMRNN produces a slightly higher SPI-3 RMSE than a standard GRU (1.339 vs. 1.338 in Taiwan). Far from being a weakness, this smoothing effect is an operational asset and should be interpreted as such. SPI-3 is defined as a *three-month* cumulative anomaly; its skill is not evaluated at individual time steps but over an integration window. A model whose hidden-state trajectory is backward-coherent suppresses step-to-step erratic transitions, producing a smoother SPI-3 time series that is less susceptible to transient dry spells incorrectly flagging drought onset. The trade-off is quantitatively favourable: a $< 0.1\%$ increase in SPI-3 RMSE (1.339 vs. 1.338) in exchange for a threefold reduction

in false-alarm ratio (Table 8, CHIRPS-TW: FAR 0.07 vs. 0.20 for CUSUM on SPI-3). Operational forecasters calibrating the SR threshold should treat this smoothing as a feature — it reduces the variance of r_t under the null, making the ARL_0 calibration more stable and the threshold B^* more transferable across years and seasons.

Calibration held-out period selection. The Shiryaev–Roberts threshold B^* is calibrated on held-out pre-event climatology (Section 3). For reproducibility, the held-out selection follows three rules. First, any year overlapping a declared drought or flood event is excluded from the calibration window to prevent leakage of event-period r_t statistics into the null distribution. Second, for each domain a minimum of five consecutive climatologically normal years is required for the calibration window; if fewer are available in the training record, the calibration bootstraps are drawn with replacement from the available years with a block length of 90 days to preserve seasonal autocorrelation. Third, the calibrated B^* is validated by a held-out climatology year (different from the calibration window) to confirm that the empirical ARL_0 is within 10% of the target value before operational deployment. The three held-out windows used in this study are: Taiwan CWA (2013–2022 training): calibration on 2013–2016, validation on 2017; CHIRPS domains (1981–2018 training): calibration on 1981–2010, validation on 2011–2015; GHCN Texas (1981–2018 training): calibration on 1981–2005, validation on 2006–2010. Event years excluded from all three: 2020–2021 (Taiwan drought), 2023 (Typhoon Haikui), 2010–2015 (Texas drought), 2015 and 2018 (Texas floods), 2016–2017 and 2021–2022 (Horn of Africa droughts).

7.2 Limitations and operational extensions

Euclidean spatial neighbourhood. The neighbourhood \mathcal{S}_ρ is defined by Euclidean distance and does not respect orographic barriers. For Taiwan’s Central Mountain Range, stations separated by only 10 km on opposite slopes occupy entirely different precipitation regimes; including both in \mathcal{S}_ρ forces the backward projector g_ϕ to approximate the reverse-martingale property across two physically independent dynamic systems simultaneously, which is why CRPS degrades above $\rho = 10$ km in the Tamsui experiment (Table 6). A graph-based neighbourhood informed by terrain-weighted proximity — replacing great-circle distance with effective flow-path distance derived from a digital elevation model (DEM) — is the natural extension. Concretely, one would define $\mathcal{S}_\rho = \{i : d_{\text{flow}}(i, i_0) \leq \rho\}$ where d_{flow} is the topographic path length along the drainage network, which automatically excludes cross-ridge stations that lie within Euclidean radius but outside the hydrological catchment. This is the most important open architectural problem for deploying RMRNN in complex terrain.

Dynamic neighbourhood radius. A complementary extension is to make ρ adaptive rather than fixed. Two natural adaptation strategies arise from the application context. First, *network-density adaptation*: in sparse networks such as GHCN Texas (52 stations over $\sim 10,000$ km²), a fixed small ρ may yield fewer than three neighbours per target site, destabilising the hidden-state summary; a minimum- k -neighbours rule with $k \geq 5$ would set ρ dynamically to the k -th nearest-neighbour distance. Second, *synoptic-scale adaptation*: the spatial coherence of precipitation anomalies differs systematically between convective and frontal regimes, so a larger neighbourhood ($\rho \approx 50$ km) is appropriate during synoptic-scale drought episodes while a small neighbourhood ($\rho \approx 5$ km) is optimal for localised flash-flood events. Conditioning ρ on a low-dimensional weather-

type index (e.g., the k -means cluster of 850-hPa vorticity over the domain) would capture this regime dependence without requiring separate model training per regime.

Stationarity of the null distribution. The SR calibration assumes that the null distribution of r_t is stable across seasons, which is violated in environments with pronounced dry and wet seasons. On the Horn of Africa, where the dry season produces near-zero P_t and correspondingly anomalous r_t spikes even during climatologically normal years, a single null mean μ_0 simultaneously overestimates the typical null residual during the dry period and underestimates it during the wet season. The consequence is an inflated false-alarm ratio at the wet-to-dry transition and a depressed detection rate at wet-season onset.

A practical remedy is a *regime-conditional null*:

$$z_t = \max\left(0, \frac{r_t - \mu_0(m_t)}{\sigma_0(m_t)}\right), \quad m_t \in \{1, \dots, 12\},$$

where $\mu_0(m)$ and $\sigma_0(m)$ are the climatological residual mean and standard deviation for calendar month m , estimated on the pre-event training window. This requires only 12 additional scalar pairs per domain and adds no model parameters. For the Horn of Africa, where the current miss rate is 0.16 at the $ARL_0 = 500$ day target, a regime-conditional z_t no longer needs to overcome the seasonal variation in r_t before reflecting genuine drought onset; we expect the miss rate to fall to $\lesssim 0.10$ without sacrificing the detection-rate advantage. On Taiwan, where seasonality in r_t is weaker (the typhoon season modulates precipitation intensity rather than presence), the seasonal correction will have a smaller but still measurable impact on calibration.

Online streaming and sliding-window approximation. Computing \mathcal{L}_{RM} requires the full hidden-state sequence $\{h_t\}_{t=1}^T$, which prevents true online training. A sliding-window approximation replaces the full sequence with a ring buffer of the W most recent states, yielding the windowed loss

$$\mathcal{L}_{\text{RM}}^{(W)}(\theta, \phi; t) = \frac{1}{W-1} \sum_{s=t-W+1}^{t-1} \|h_s - g_\phi(h_{s+1})\|^2,$$

where only W consecutive hidden states need to be retained (memory $O(Wd)$). At $W = 168$ (one week of hourly data) and $d = 64$ this is less than 0.1 megabytes (MB) per target cell. Validating this approximation requires verifying two properties: (i) that the backward projector g_ϕ trained with $\mathcal{L}_{\text{RM}}^{(W)}$ converges to the same fixed point as the full-sequence version, and (ii) that the SR statistic built on windowed residuals preserves the target ARL_0 calibration. Preliminary theory suggests that $W \geq 3\tau_{\text{corr}}$ (three auto-correlation timescales of r_t) is sufficient for property (ii); for the Taiwan CWA domain $\tau_{\text{corr}} \approx 24$ h gives a minimum window of $W = 72$ steps, and the buffer $W = 168$ provides a conservative safety margin with little memory cost.

ERA5-Land latency and Integrated Forecasting System (IFS) substitution. Operational deployment requires real-time ingestion of ERA5-Land reanalysis, which carries a 4–5 day latency due to the observation assimilation cycle. For drought detection, where the SR detector produces alerts 8–12 days before SPI-3 crossing, this latency is not operationally limiting: a 5-day-lagged ERA5-Land input is still available several days before the alert window. For flash-flood early warning, however, the 4–5 day latency is incompatible with the 3–6 hour alarm horizon demonstrated in the Haikui case study, and substitution with IFS operational analysis — available with < 6 h latency after the analysis cycle — is essential.

The key technical question for the IFS substitution is whether the backward projector g_ϕ , trained on ERA5-Land (a reanalysis product with distinct bias structure and spatial interpolation from IFS operational output), can be applied to IFS fields at inference time. Two strategies are feasible: (a) *domain adaptation*, in which g_ϕ is fine-tuned on a short archive of matched ERA5-Land/IFS pairs to correct systematic offsets; (b) *quantile mapping*, in which IFS fields are remapped to ERA5-Land marginal distributions as a pre-processing step before entering the model. Both are low-cost extensions of the current pipeline and are the subject of planned follow-up work.

What the RM framework cannot do, and the hybrid extension. RMRNN improves the *statistical structure* of the hidden-state trajectory but cannot create physical predictability where none exists. In the Horn of Africa, where the short-rain season onset is driven by Intertropical Convergence Zone (ITCZ) migration and Indian Ocean sea-surface temperature gradients at synoptic to intraseasonal scales, the information needed to predict drought onset more than two weeks ahead is not present in the local $\rho = 50$ km neighbourhood; no regularization of the hidden state can recover it. The RM framework’s contribution in such settings is to separate *predictable* regime change (where r_t inflates gradually, driven by multi-channel anomalies) from *unpredictable* but genuine change (where r_t inflates abruptly, after the event has already begun), and to provide a statistically principled alarm for both.

The natural remedy for the missing large-scale information is *hybrid feature engineering*: augmenting the local input x_t with large-scale climate indices as additional scalar channels. For the Horn of Africa domain, the most physically relevant supplementary predictors are:

- *Indian Ocean Dipole (IOD) index* represented by the Dipole Mode Index (DMI_t): positive IOD events systematically suppress the short rains over East Africa by weakening the onshore moisture flux from the western Indian Ocean [28];
- *El Niño–Southern Oscillation (ENSO) state* represented by the Niño-3.4 sea-surface temperature (SST) anomaly (N34_t): El Niño modulates ITCZ positioning and the Walker circulation, driving interannual variability in the Horn of Africa long rains [27];
- *Madden–Julian Oscillation (MJO) phase* represented by the Real-time Multivariate MJO indices (RMM1/RMM2): 30–60 day intraseasonal modulation of East African rainfall.

These indices are available in near-real time (IOD: NOAA Extended Reconstructed Sea Surface Temperature version 5 [ERSSTv5]; ENSO: Climate Prediction Center [CPC]; MJO: Bureau of Meteorology) and can be appended to x_t as additional scalar channels without any architectural change to RMRNN — because the RM loss operates on $h_t \in \mathbb{R}^d$ regardless of input dimensionality (Section 4.5). For the Taiwan drought domain, analogous large-scale predictors include the Western Pacific subtropical high ridge-line index and the East Asian summer monsoon intensity index [29], which govern typhoon track and landfall probability and therefore modulate the reservoir refill cycle central to operational drought management.

The implementation workflow for a practitioner wishing to apply this hybrid extension requires three steps. First, download the chosen indices at daily or weekly resolution from their respective operational archives (IOD: NOAA ERSSTv5; ENSO Niño-3.4: NOAA CPC; MJO RMM1/RMM2: Bureau of Meteorology; Taiwan western North Pacific subtropical high [WNPSH] and East Asian summer monsoon [EASM] indices: Japan

Meteorological Agency [JMA]). Second, append each index as an additional scalar channel to x_t in (1); no change to the RMRNN architecture is needed because the RM loss acts on the hidden state $h_t \in \mathbb{R}^d$ regardless of input width. Third, retrain with the same $\mathcal{L}_{\text{total}}$ objective, fixing all hyperparameters as in Section 3 and using the same 1,000-replication purged-block bootstrap protocol described in Section 4. For the Horn of Africa, where the current miss rate at $\text{ARL}_0 = 500$ days is 0.16, the IOD and Niño-3.4 channels are expected to provide the largest single-index gains because they encode the large-scale ITCZ and moisture-flux signals that drive interannual variability at lead times beyond the local $\rho = 50$ km neighbourhood. A prospective evaluation with independent drought seasons would be needed before these large-scale indices could be recommended for operational warning use.

7.3 Implications for hydrometeorological forecasting and warning

Taken together, the numerical experiments suggest five implications for hydrometeorological forecasting and warning systems.

(i) The warning residual can be climatologically calibrated. A vanilla GRU’s residual $\hat{P}_t - P_t$ has a complex null distribution that mixes irreducible precipitation variability, model bias, and representational drift. RMRNN decomposes this into a task residual (which remains complex) and a defect r_t whose null distribution is right-skewed but stable under the no-change climatology, with location and scale parameters (μ_0, σ_0) and the normalizing function ψ_0 estimated from pre-event climatology. The SR detector exploits this calibration to achieve the $3\times$ FAR reduction reported in Tables 8 and 9.

(ii) Backward coherence encodes multi-channel regime state. The 8–12 day drought-detection lead advantage over SPI-3 is not achievable by any detector operating on precipitation alone, because precipitation deficits large enough to cross the SPI-3 threshold take 8–12 weeks to accumulate. RMRNN detects the onset earlier because r_t integrates vorticity, temperature, and moisture anomalies that precede the precipitation anomaly. This is a new use of the reverse-martingale framework: the hidden state as a *multi-channel atmospheric state estimator* whose deviation from its trained null is a regime-change alarm.

(iii) Warning gains can occur without degrading forecast skill. Across all five forecasting benchmarks, the difference in CRPS between RMRNN and GRU is ≤ 0.007 in the reported tables, indicating that backward coherence is obtained with only a small forecast-skill cost in these experiments. This separates the RMRNN contribution from regularization methods (dropout, L^2 weight decay, spectral normalization) that also affect task accuracy.

(iv) The spatial scale of the reverse-martingale property is identifiable and physically interpretable. The ρ -sensitivity experiment (Table 6) reveals a clear optimum at $\rho = 5$ km for the Tamsui basin, with performance degrading monotonically above $\rho \approx 10$ km. This supports the interpretation that the backward-coherence signal is spatially bounded by the orographic scale of the catchment.

(v) The approach is compatible with multi-variable predictors. The ERA5-Land result (Table 7) supports the interpretation that expanding the input from 1 variable (precipitation) to 5 variables does not change the RM computational overhead and preserves the backward-coherence property. This makes RMRNN a candidate for future testing with kilometre-scale multi-variable NWP products.

The contribution of this work includes the spatial forward information set (2), the residual-based SR detector (Algorithm 1), the small-area observational benchmark (Table 1), and the case-study demonstration of operational lead-time gain across Taiwan, the Horn of Africa, and Texas.

8 Conclusions

This study evaluated a reverse-martingale regularized recurrent network (RMRNN) as a coupled precipitation-forecasting and early-warning system for small-area hydrometeorology. The main result is practical rather than only methodological: the hidden-state regularizer can be added without materially degrading standard precipitation forecast scores, while the resulting residual process provides a calibrated basis for drought and flood alarms.

Forecasting. Across five benchmarks (Tamsui, Zhuoshui, CHIRPS Taiwan, CHIRPS Horn of Africa, ERA5-Land Taiwan), each evaluated over 1,000 replications, RMRNN matches or slightly improves GRU CRPS at hourly and daily lead times (Tamsui: CRPS 0.379 \rightarrow 0.379; CHIRPS-HoA: 0.867 \rightarrow 0.866; ERA5-Land: 0.606 \rightarrow 0.603). The spatial neighbourhood radius ρ has an interior optimum near 5 km for the Tamsui basin (CRPS 0.321 at $\rho = 5$ km, rising to 0.380 at $\rho = 50$ km), consistent with a local-information trade-off: adding nearby stations helps until the neighbourhood begins to mix different orographic or convective regimes.

Warning performance. The SR detector on RMRNN residuals reduces false-alarm ratios to 7–9% for drought detection and 7–8% for flash-flood detection across the precipitation domains, compared with 20–24% for CUSUM on SPI-3 and 27–34% for raw precipitation thresholding. Detection rates simultaneously improve by 6–12 percentage points. These gains are reported in operational units through calibrated ARL_0 targets, so the warning rule can be interpreted as a controllable trade-off between lead time and false alarms.

Case studies. On the 2020–2021 Taiwan drought, the SR detector flagged onset on 12 July 2020 — **10 days earlier than SPI-3** and 14 days earlier than the CWA declaration — with zero false alarms in the preceding 36 months. On Typhoon Haikui (September 2023), the detector triggered at 21:30 UTC on 4 September — **4 hours before the CWA alert** and 6.5 hours before peak basin rainfall — with only 2 false alarms compared with 5 for the CWA operational system and 14 for a raw precipitation threshold over the 2013–2022 calibration period.

Operational implication. The ERA5-Land multi-variable benchmark suggests that the RM overhead (one backward-projector forward pass per time step) does not grow with the number of meteorological predictors, because the backward projector operates on the hidden state $h_t \in \mathbb{R}^d$. This makes the approach suitable for future evaluation with larger reanalysis or numerical weather prediction feature sets, provided that site-specific calibration and independent event validation are retained.

All experiments report mean \pm SD across 1,000 replications. The reference implementation, data-processing pipeline, and experiment scripts are released at <https://github.com/ycchang/RMRNN>.

A Reverse-martingale formulation and implementation details

A.1 Formal reverse-martingale motivation

A sequence $\{M_t\}$ adapted to a decreasing filtration $\mathcal{G}_t \supset \mathcal{G}_{t+1}$ is a reverse martingale [1] if M_t is \mathcal{G}_t -measurable and

$$\mathbb{E}[M_t | \mathcal{G}_{t+1}] = M_{t+1}.$$

For a finite hidden-state trajectory we use the decreasing future sigma-field $\mathcal{G}_t^{(h)} = \sigma(h_s : s \geq t)$ as the formal motivation. The one-step projector $g_\phi(h_{t+1})$ is a Markov approximation to the generally richer conditional expectation $\mathbb{E}[h_t | \mathcal{G}_{t+1}^{(h)}]$. The hidden states of a trained recurrent network do not satisfy this identity exactly. The role of \mathcal{L}_{RM} in (3) is therefore not to impose a literal martingale model on precipitation, but to make the learned representation approximately backward coherent during ordinary climatological periods. When this coherence holds, the defect r_t in (5) has a stable null distribution that can be calibrated on pre-event climatology and then monitored by the SR statistic in (6).

A.2 Backward projector and training schedule

In all experiments the backward projector has residual form

$$g_\phi(h) = h + W_2 \text{ReLU}(W_1 h + b_1) + b_2.$$

The matrix W_1 is Xavier-initialised, while W_2 and b_2 are initialised at zero so that $g_\phi(h) = h$ at epoch 0 but gradients can still enter the residual branch. This prevents the auxiliary RM loss from destabilising early task learning. The RM penalty is introduced after $K_0 = 5$ warm-up epochs and decayed from $\lambda_0 = 0.1$ to 0.01 by the final epoch, as shown in (4). Gradients are computed by standard backpropagation through time (BPTT). The same projector is used with Elman, LSTM, and GRU cells; for gated cells it acts only on the exposed hidden state h_t , not on the internal gate variables.

A.3 Interpretation of backward coherence

A standard GRU minimises prediction error at each step but imposes no discipline on the relationship between neighbouring hidden states. Consequently, two consecutive weather states can occupy unrelated regions of \mathbb{R}^d even when the observed atmosphere evolves smoothly. RM regularization adds the requirement that h_t be approximately reconstructable from h_{t+1} through g_ϕ . Normal high-pressure, monsoon, or weak-rainfall regimes should then move through hidden space by small, regular steps, while genuine meteorological shifts should produce larger departures. The empirical aggregate defect $\hat{Q} = \sum_{t=1}^{T-1} \|\delta_t\|^2$ measures aggregate non-coherence over a sequence and equals $(T-1)\mathcal{L}_{\text{RM}}$ on the observed hidden-state path. In the main text, the empirical evidence for this interpretation is the improved false-alarm control of the SR detector without a corresponding loss of forecast skill.

Data availability

CWA rain-gauge and ASOS data are available upon request from the Taiwan Central Weather Administration. CHIRPS v2 is available from the Climate Hazards Center (<https://www.chc.ucsb.edu/data/chirps>). GHCN-Daily is available from NOAA (<https://www.ncei.noaa.gov/products/land-based-station/global-historical-climatology-network-daily>). ERA5-Land is available from the Copernicus Climate Data Store (<https://cds.climate.copernicus.eu/>). All code and experiment scripts are released at <https://github.com/ycchang/RMRNN>.

Acknowledgments

This work was supported by the National Science and Technology Council (NSTC) of Taiwan under the RMRNN project. We thank the Taiwan Central Weather Administration for rain-gauge data access.

References

- [1] Doob, J. L., 1953: *Stochastic Processes*. Wiley, 654 pp.
- [2] Cho, K., B. van Merriënboer, C. Gulcehre, D. Bahdanau, F. Bougares, H. Schwenk, and Y. Bengio, 2014: Learning phrase representations using RNN encoder–decoder for statistical machine translation. *Proc. 2014 Conf. Empirical Methods in Natural Language Processing*, Doha, Qatar, Association for Computational Linguistics, 1724–1734, doi:10.3115/v1/D14-1179.
- [3] Hochreiter, S., and J. Schmidhuber, 1997: Long short-term memory. *Neural Comput.*, **9**, 1735–1780, doi:10.1162/neco.1997.9.8.1735.
- [4] Espeholt, L., and Coauthors, 2022: Deep learning for twelve hour precipitation forecasts. *Nat. Commun.*, **13**, 5145.
- [5] Funk, C., and Coauthors, 2015: The climate hazards infrared precipitation with stations—a new environmental record for monitoring extremes. *Sci. Data*, **2**, 150066.
- [6] Gama, J., I. Žliobaitė, A. Bifet, M. Pechenizkiy, and A. Bouchachia, 2014: A survey on concept drift adaptation. *ACM Comput. Surv.*, **46**(4), Article 44, 37 pp.
- [7] Hersbach, H., and Coauthors, 2020: The ERA5 global reanalysis. *Quart. J. Roy. Meteor. Soc.*, **146**, 1999–2049.
- [8] Hundman, K., V. Constantinou, C. Laporte, I. Colwell, and T. Soderstrom, 2018: Detecting spacecraft anomalies using LSTMs and nonparametric dynamic thresholding. *Proc. 24th ACM SIGKDD*, 387–395.
- [9] Milly, P. C. D., J. Betancourt, M. Falkenmark, R. M. Hirsch, Z. W. Kundzewicz, D. P. Lettenmaier, and R. J. Stouffer, 2008: Stationarity is dead: Whither water management? *Science*, **319**, 573–574.
- [10] López de Prado, M., 2018: *Advances in Financial Machine Learning*. Wiley.

- [11] Roe, G. H., 2005: Orographic precipitation. *Annu. Rev. Earth Planet. Sci.*, **33**, 645–671.
- [12] McKee, T. B., N. J. Doesken, and J. Kleist, 1993: The relationship of drought frequency and duration to time scales. *Proc. 8th Conf. on Applied Climatology*, Anaheim, CA, AMS, 179–184.
- [13] Menne, M. J., I. Durre, R. S. Vose, B. E. Gleason, and T. G. Houston, 2012: An overview of the Global Historical Climatology Network-Daily database. *J. Atmos. Oceanic Technol.*, **29**, 897–910.
- [14] Moustakides, G. V., 1986: Optimal stopping times for detecting changes in distributions. *Ann. Statist.*, **14**, 1379–1387.
- [15] Muñoz-Sabater, J., and Coauthors, 2021: ERA5-Land: A state-of-the-art global reanalysis dataset for land applications. *Earth Syst. Sci. Data*, **13**, 4349–4383.
- [16] Pollak, M., 1985: Optimal detection of a change in distribution. *Ann. Statist.*, **13**, 206–227.
- [17] Pollak, M., 1987: Average run lengths of an optimal method of detecting a change in distribution. *Ann. Statist.*, **15**, 749–779.
- [18] Ravuri, S., and Coauthors, 2021: Skilful precipitation nowcasting using deep generative models of radar. *Nature*, **597**, 672–677.
- [19] Ronneberger, O., P. Fischer, and T. Brox, 2015: U-Net: Convolutional networks for biomedical image segmentation. *Medical Image Computing and Computer-Assisted Intervention – MICCAI 2015*, Lecture Notes in Computer Science, **9351**, 234–241.
- [20] Shi, X., and Coauthors, 2015: Convolutional LSTM network: A machine learning approach for precipitation nowcasting. *Adv. Neural Inf. Process. Syst.*, 802–810.
- [21] Shiryaev, A. N., 1963: On optimum methods in quickest detection problems. *Theory Probab. Appl.*, **8**, 22–46.
- [22] Sloughter, J. M., A. E. Raftery, T. Gneiting, and C. Fraley, 2007: Probabilistic quantitative precipitation forecasting using Bayesian model averaging. *Mon. Wea. Rev.*, **135**, 3209–3220.
- [23] Wang, Y., M. Long, J. Wang, Z. Gao, and P. S. Yu, 2017: PredRNN: Recurrent neural networks for predictive learning using spatiotemporal LSTMs. *Adv. Neural Inf. Process. Syst.*, 879–888.
- [24] Wang, Y., H. Wu, J. Zhang, Z. Gao, J. Wang, P. S. Yu, and M. Long, 2023: PredRNN: A recurrent neural network for spatiotemporal predictive learning. *IEEE Trans. Pattern Anal. Mach. Intell.*, **45**, 2208–2225.
- [25] World Meteorological Organization, 2012: Standardized Precipitation Index User Guide. WMO-No. 1090, 24 pp.
- [26] Lorenz, E. N., 1969: The predictability of a flow which possesses many scales of motion. *Tellus*, **21**, 289–307.

- [27] Nicholson, S. E., 2017: Climate and climatic variability of rainfall over eastern Africa. *Rev. Geophys.*, **55**, 590–635.
- [28] Saji, N. H., B. N. Goswami, P. N. Vinayachandran, and T. Yamagata, 1999: A dipole mode in the tropical Indian Ocean. *Nature*, **401**, 360–363.
- [29] Wang, B., R. Wu, and K.-M. Lau, 2001: Interannual variability of the Asian summer monsoon: contrasts between the Indian and the western North Pacific–East Asian monsoons. *J. Climate*, **14**, 4073–4090.